Nano Today 61 (2025) 102633

Contents lists available at ScienceDirect

Nano Today

journal homepage: www.elsevier.com/locate/nanotoday

Optically-modulated and mechanically-flexible MXene artificial synapses with visible-to-near IR broadband-responsiveness

Chung Won Lee [a], Seung Ju Kim [b], Han-Kyun Shin [a,c], Young-Jun Cho [c], Changhyeon Yoo [a], Sang Sub Han [a], Hyo-Jong Lee [c], Jung Han Kim [c], Yeonwoong Jung [a,d,e,*]

[a] NanoScience Technology Center, University of Central Florida, Orlando, FL 32826, United States
[b] The Department of Electrical and Computer Engineering, University of Southern California, Los Angeles, CA 90089, United States
[c] Department of Materials Science and Engineering, Dong-A University, Busan 49315, South Korea
[d] Department of Materials Science and Engineering, University of Central Florida, Orlando, FL 32816, United States
[e] Department of Electrical and Computer Engineering, University of Central Florida, Orlando, FL 32816, United States

ARTICLE INFO

Keywords:
MXene
Flexible device
Optoelectronic device
Optical synapse
Neuromorphic computation
Artificial neural network

ABSTRACT

The inherent limitations of von Neumann computing associated with its inefficient parallel-processing of massive data become increasingly pronounced in state-of-the-art digital device technologies. Artificial synapses of the human brain-inspired neuromorphic computing are emerging as a viable solution, which demands to explore unconventional materials responsive to a variety of electrical and/or optical stimuli. Herein, we report that solution-processed titanium carbide MXene ($Ti_3C_2T_x$) exhibits essential characteristics for optoelectronic synapses-based neuromorphic computing. Specifically, it presents optically-triggered synaptic plasticity with memory effects in a broad spectral range, as well as accompanying a large degree of mechanical deformability. By leveraging the optoelectronics-mechanics coupling, we demonstrate that MXene-based devices can simulate vital functionalities demanded in artificial neural networks (ANNs) such as associative learning behaviors and high-accuracy pattern recognition. Furthermore, the operational principle of the MXene optoelectronic synapses is unveiled in the context of the charge trapping/de-trapping mechanism enabled by its processing-introduced bandgap opening.

Introduction

The advent of the artificial intelligence (AI) era has revolutionized the processing of massive and complex data for associative learning and recognition in advanced computing technologies by enhancing the linearity and symmetric conductance [1]. The conventional digital approaches based on von Neumann architectures are facing significant limitations due to various factors such as physical memory separation and overabundant energy consumption [2–5]. To overcome the hurdles, a concept of the biologically-inspired neuromorphic computation has emerged, offering distinct advantages of low-energy and high-speed operations [6–12]. Artificial synaptic devices enabling the neuromorphic operations have been extensively explored, mostly adopting electrically-modulated stimuli and their responsive materials [13,14]. However, this solitary electrical process exhibits technical difficulties such as interconnection issues and/or bandwidth-connection-density trade-offs, imposing restrictions on device performances [15,16]. Inspired by the challenges, optoelectronic synapses operating by translating optical stimuli to electrical signals have arisen, which simulate the visual perception process of biological synapses for computations [17–20]. Furthermore, their advances often demand additional functionalities into the optically-responsive materials toward unconventional yet transformative neuromorphic performances. Amongst a variety of the optical building-block materials, MXene in a general form of $M_{n+1}X_nT_x$ where M is a transition metal, X is C or N, and T_x represents surface terminations, are projected to offer a number of advantages [21,22]. Unlike covalently-bonded thin films for conventional devices, MXenes present a large degree of structure-processing-property tunability due to their structural anisotropy and predictable electrical/optical properties with modulated functional groups [23,24]. This intrinsic superiority of MXenes coupled with their solution-based processability is projected to render opportunities for neuromorphic applications [25,26], which, however, have remained largely unexplored in terms of optoelectronics. Herein, we explore MXene ($Ti_3C_2T_x$)-based

* Corresponding author at: NanoScience Technology Center, University of Central Florida, Orlando, FL 32826, United States.
E-mail address: yeonwoong.jung@ucf.edu (Y. Jung).

https://doi.org/10.1016/j.nantod.2025.102633
Received 27 September 2024; Received in revised form 15 December 2024; Accepted 5 January 2025
Available online 10 January 2025

optoelectronic artificial synapses and their implications for neuromorphic devices. Solution-processed MXenes integrated on flexible polyimide (PI) substrates exhibit broadband photo-responsiveness with memory effects in a spectral range of visible-to-near infrared (IR). Notably, these characteristics are utilized to demonstrate an essential set of synaptic plasticity, i.e., excitatory/inhibitory postsynaptic current (EPSC/IPSC), paired-pulse facilitation (PPF), short-term potentiation/depression (STP/STD), long-term potentiation/depression (LTP/LTD), and short-term to long-term memory transition (STM-to-LTM). These comprehensive features are employed for two different neuromorphic applications; (1) synaptic simulations of pattern/image recognition for ANNs, achieving a deformation-independent high accuracy of ~90 %. (2) demonstrations of Pavlovian conditioning estimations for associative learning behaviors.

Experimental section/methods

Materials

1 g of Lithium fluoride (LiF) and 1 g of Titanium aluminum carbide (Ti_3AlC_2) powders were mixed with 12 ml of 37 % Hydrochloric acid (HCl). The mixed solution was rigorously stirred with a magnetic bar at ~500 rpm. After 36 h, the mixed solution was centrifuged (3500 rpm, 5 min for each cycle) with deionized (DI) water and it was repeatedly washed out > 5 times until the pH of the supernatant reached 6. The DI dispersed $Ti_3C_2T_x$ solution was then dried to evaporate the redundant DI water using a hot plate (>100 °C). The resulting $Ti_3C_2T_x$ powders were gathered and then dispersed into an organic solvent of N- Methylmorpholine N-oxide (NMMO) at a desired concentration of 5–10 mg/ml.

MXene ($Ti_3C_2T_x$)-based flexible device fabrication

The synthesized MXene solution was extracted with a pipette and was drop-casted onto a flexible PI substrate covering an area of 0.5 cm × 2 cm. Then, gold (Au) electrodes (75 nm thickness) were deposited onto the MXene/PI surface via RF sputtering (deposition rate:15 nm/min, deposition time: 5 min)

Material characterizations

Horiba LabRAM HR Evolution instrument was used for Raman characterizations at room temperature with a 532 nm excitation laser. XPS characterizations were performed using ESCALAB 250 (Thermo Fisher Scientific) in an ultrahigh vacuum condition (10^{-9} mBar). XRD characterizations were conducted using Empyrean PANalytical with Cu K-α (0.154060 nm) radiation. TEM/EDS images were obtained with Talos F200X (Thermo Fisher Scientific) which was operated at an acceleration voltage of 200 kV. Evolution 220 UV-Vis spectrometer was employed for acquiring optical absorbance spectra in a wavelength range of 300–1000 nm.

Optoelectronic synapse measurements

Optical illuminators of various wavelengths (405 nm; 100 mW cw laser diode light source, 625 nm; ThorlabsM625L4-C2, and 940 nm; ThorlabsM940L3-C1) were used for pulsed stimuli applications. A home-built probe station operated with a semiconductor parameter analyzer (Keysight B1500A) was employed for electrical measurements.

Computation simulations

Neuromorphic simulations were conducted based on the Multi-Layer-Perceptron (MLP) neural network. The employed handwritten digit images were composed of 28 × 28 pixels, and a total of 60,000 images were trained and 10,000 images were tested for recognition evaluations.

Results and discussion

Design of flexible $Ti_3C_2T_x$ synaptic device and characterization

Fig. 1a illustrates the fabrication process of a flexible MXene synaptic device. Lithium fluoride (LiF) and Titanium aluminum carbide (Ti_3AlC_2) powders are mixed with Hydrochloric acid (HCl), which exfoliates Ti_3AlC_2 sheets into $Ti_3C_2T_x$. The prepared solution is subsequently dissolved into an organic solvent of N-Methylmorpholine N-oxide (NMMO). The final product is drop-casted onto a flexible PI substrate, followed by a deposition of gold (Au) electrodes. Details about MXene synthesis and device fabrications are presented in the *Experimental Sections/Methods*. The thickness of MXene devices and their uniformity are highly controllable by adjusting their solution preparation conditions. In this study, micrometer-thick MXene films were deliberately employed to ensure a homogenous coverage of electrical channels between Au electrodes, thus prominent and reliable photocurrents upon optical illuminations. In fact, these devices adopting micrometer-thick films exhibit qualitatively similar synaptic plasticity characteristics driven by pulsed optical stimuli, confirmed through a number of measurements. Fig. 1b presents a Raman spectrum of MXene, displaying various peaks corresponding to the vibration modes of $Ti_3C_2T_x$ and its surface functionalization. The Raman spectrum is grouped into three regions of Ti, T_x, and C, wherein the vibrations of $Ti_2C_2T_x$ include E_g (in-plane) and $A_{1\,g}$ (out-of-plane) peaks for both Ti and C [27]. Peaks of $A_{1\,g}$ at 205 cm^{-1} and E_g at 286/404 cm^{-1} are associated with the surface groups of Ti and T_x, respectively, and both $A_{1\,g}$ and E_g peaks at 725 cm^{-1} and 580/622 cm^{-1} correspond to the C vibrations [28,29]. Fig. 1c presents a high-resolution transmission electron microscopy (HR-TEM) image of a representative sample, revealing (0110) lattice fringes of $Ti_3C_2T_x$ MXene with a measured interplanar spacing of 0.26 nm, consistent with previous TEM observations [30–32]. Interestingly, TiO_2 phases with (101) lattice fringes [33–35] are often observed within the MXene matrix, which is attributed to a spontaneous oxidation of constituent Ti associated with MXene processing steps as previously reported [36,37]. Exclusive roles of TiO_2 on resulting optoelectronic properties will be discussed in details later. Fig. 1d displays a selective area electron diffraction (SAED) pattern corresponding to the MXene phase in Fig. 1c. Additional TEM characterizations confirm the presence of residual Ti_3AlC_2 not fully exfoliated into $Ti_3C_2T_x$ MXene (Supporting Information, Fig. S1). Furthermore, scanning electron microscopy (SEM) and energy dispersive x-ray spectroscopy (EDS) characterizations verify a homogeneous distribution of elements within MXene (Supporting Information, Fig. S2).

Optical synaptic plasticity characteristics of $Ti_3C_2T_x$-based flexible device

The artificial synaptic properties of MXene devices were characterized under a sequential application/termination of optical pulse stimuli. According to the synaptic operation model of mimicking the brain's memory learning/forgetting process by Atkinson and Shiffrin, stimuli as described perceptions are received by respective organs and their resulting signals are subsequently registered into sensory memories [38]. In this process, the stimuli are converted into STM lasting for seconds-to-minutes, which can be spontaneously transited to LTM lasting for minutes-to-years unless the organs are repeatedly provided with the intended information [39]. Accordingly, the instantaneous stimuli must be frequently applied in a few second durations to ensure memorizing the information. Therefore, it is crucial to demonstrate this synaptic plasticity-driven STM-to-LTM transition in simulating the entire learning/forgetting process of artificial synapses. The demonstrations were performed with MXene devices by stimulating them with adjusted optical pulses, and the resulting synaptic properties are manifested by their electrical responses [40,41]. Fig. 2a-c present STP characteristics of a representative device under illuminations at three different wavelengths of 405, 625, and 940 nm. Fig. 2a displays pulse number

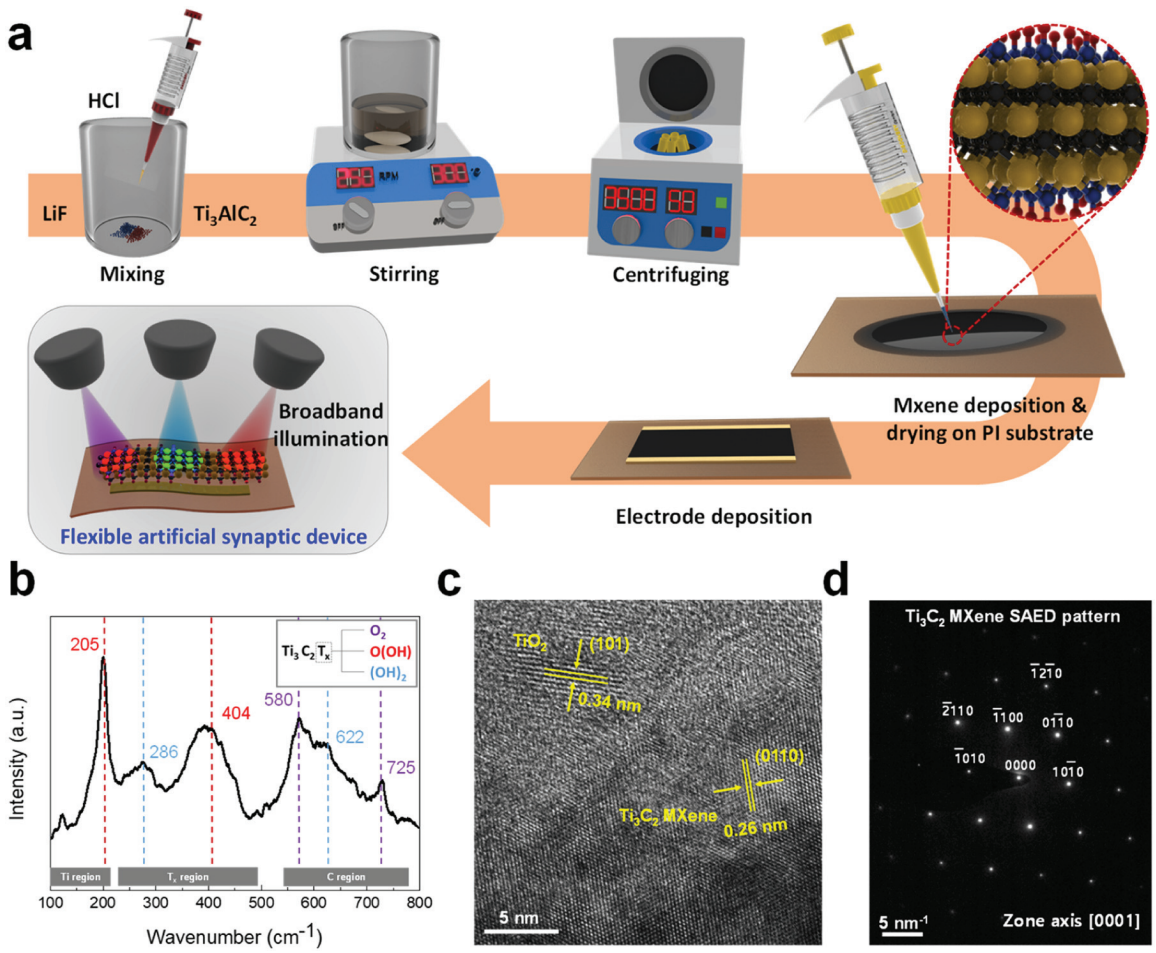

Fig. 1. Fabrication of $Ti_3C_2T_x$-based optoelectronic device and material characterization. (a) Synthesis flow of $Ti_3C_2T_x$ MXene and its integration for flexible optoelectronic device. (b) Raman spectrum, (c) HR-TEM image, and (d) SAED pattern obtained from MXene samples.

(n)-dependent STP characteristics under optical pulses at 405 nm, measured with varying bias voltages (duration time t = 0.5 s for each pulse). Fig. 2b and 2c demonstrate that qualitatively similar STP characteristics are observed with wavelengths of 625 and 940 nm, respectively. Furthermore, in all three wavelengths, LTD characteristics are also observed once the optical stimulus is terminated, which are manifested by the spontaneous long-term decay of the potentiated current. Fig. 2d-f present bias voltage-dependent STP/LTD characteristics of the device at a fixed pulse number, n = 5. Similar characteristics are observed irrespective of the wavelength variation, i.e. 405 (Fig. 2d), 625 (Fig. 2e), and 940 nm (Fig. 2f), respectively. PPF is a vital parameter employed for identifying STP features as well, which is defined to be the ratio of EPSC obtained from an application of two consecutive stimuli [42,43]. Fig. 2g-i depict the PPF indexing for the identical device, manifested by EPSC changes under initial (A_1) and secondary (A_2) stimuli. The device was illuminated with 1 s on/off intervals at wavelengths of 405 (Fig. 2g), 625 (Fig. 2h), and 940 nm (Fig. 2i), respectively. The synaptic plasticity of the device is further evaluated by plotting PPF indexing vs. interval (Δt) between two successive stimuli. Fig. 2j-l present PPF indexing plots of the same device under illuminations at 405 (Fig. 2j), 625 (Fig. 2k), and 940 nm (Fig. 2l), respectively. The fitting curves were derived from Eq. (1) [44],

$$PPF\text{index} = c_1 \bullet \exp\left(\frac{\Delta t}{\tau_1}\right) + c_2 \bullet \exp\left(\frac{\Delta t}{\tau_2}\right) + 1 \quad (1)$$

where the relaxation time features τ_1 (or τ_2) which indicates the fast (or slow) phase of PPF index, respectively. The magnitude of the fast (or slow) phase is implied by c_1 (or c_2) which corresponds to initial facilitation values. In general, τ_2 is notably larger than τ_1, which is indicative of successive synaptic operations [45]. The PPF indexing values for wavelengths 405, 625, 940 nm and t = 0.5, 1, 2, 3, 4, 5, 10, 15, 20 s are as follows; (1) For 405 nm; 1.360, 1.215, 1.156, 1.100, 1.083, 1.039, 1.003, 0.997, 0.994. (2) For 625 nm; 1.672, 1.444, 1.394, 1.281, 1.263, 1.252, 1.141, 1.076, 0.952, and (3) For 940 nm; 1.716, 1.546, 1.392, 1.342, 1.213, 1.236, 1.177, 1.110, 1.021, respectively. Overall, these comprehensive data in Fig. 2a-l confirm that MXene devices can successfully function as artificial synapses by simulating the human brain's operational principles under broadband stimuli.

Mechanical robustness of flexible $Ti_3C_2T_x$-based optoelectronic device

Beyond confirming the intrinsic synaptic plasticity of MXenes, we leveraged their solution process-enabled mechanical deformability toward flexible optoelectronic synaptic devices. Fig. 3a shows snapshot images of a device undergoing a systematic mechanical bending with increasing bending radii. The calculated bending strain values from the left-to-right, are 0.23, 0.33, 0.43, and 0.52 %, respectively. Fig. 3b presents the trend of PPF values of the same device with varying strain values under three different wavelengths of 405, 625, and 940 nm. The positive and negative strain values represent "upward bending" and "downward folding," respectively. The PPF indexing values remain consistent across all three wavelengths throughout the strain change of ~1.04 %. This mechanical robustness of the device and its associated coupling to optical synapses were further evaluated under harsh mechanical conditions. Specifically, the device was subjected to an iterative application of bending/releasing for a total of 1000 cycles with a

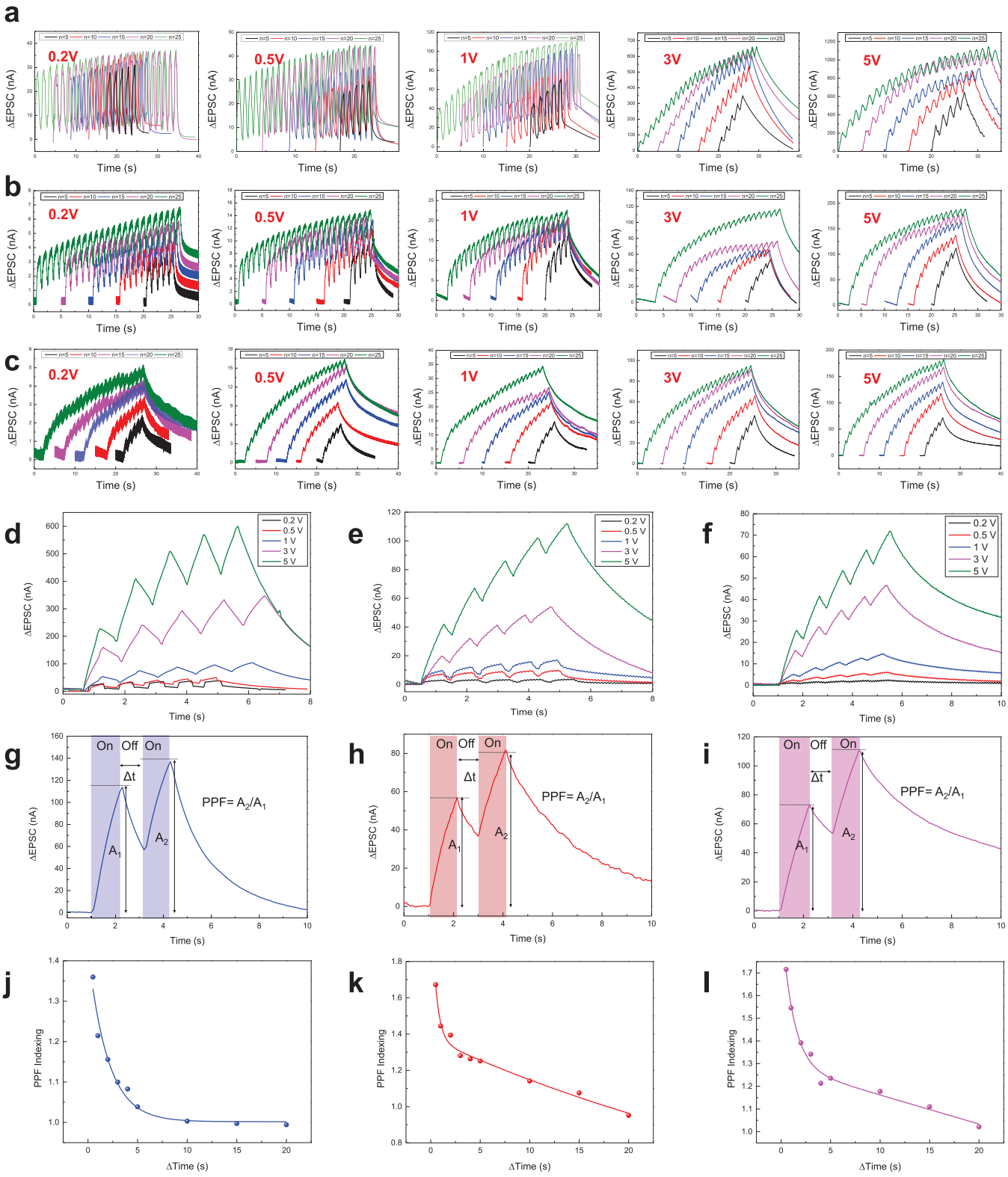

Fig. 2. Optical synaptic plasticity characteristics of $Ti_3C_2T_x$-based optoelectronic device. (a-c) STP and LTD characteristics for pulse numbers of n = 5, 10, 15, 20, 25 under optical illuminations at wavelengths of; (a) 405 nm, (b) 625 nm, and (c) 940 nm. (d-f) STP and LTD characteristics for n = 5 under varying bias voltages at wavelengths of; (d) 405 nm, (e) 625 nm, and (f) 940 nm. (g-i) PPF indexing plots with intervals of Δt = 1 s obtained from wavelengths of; (g) 405 nm, (h) 625 nm, and (i) 940 nm. (j-l) PPF index vs. varying Δt obtained from wavelengths of; (j) 405 nm, (k) 625 nm, and (l) 940 nm.

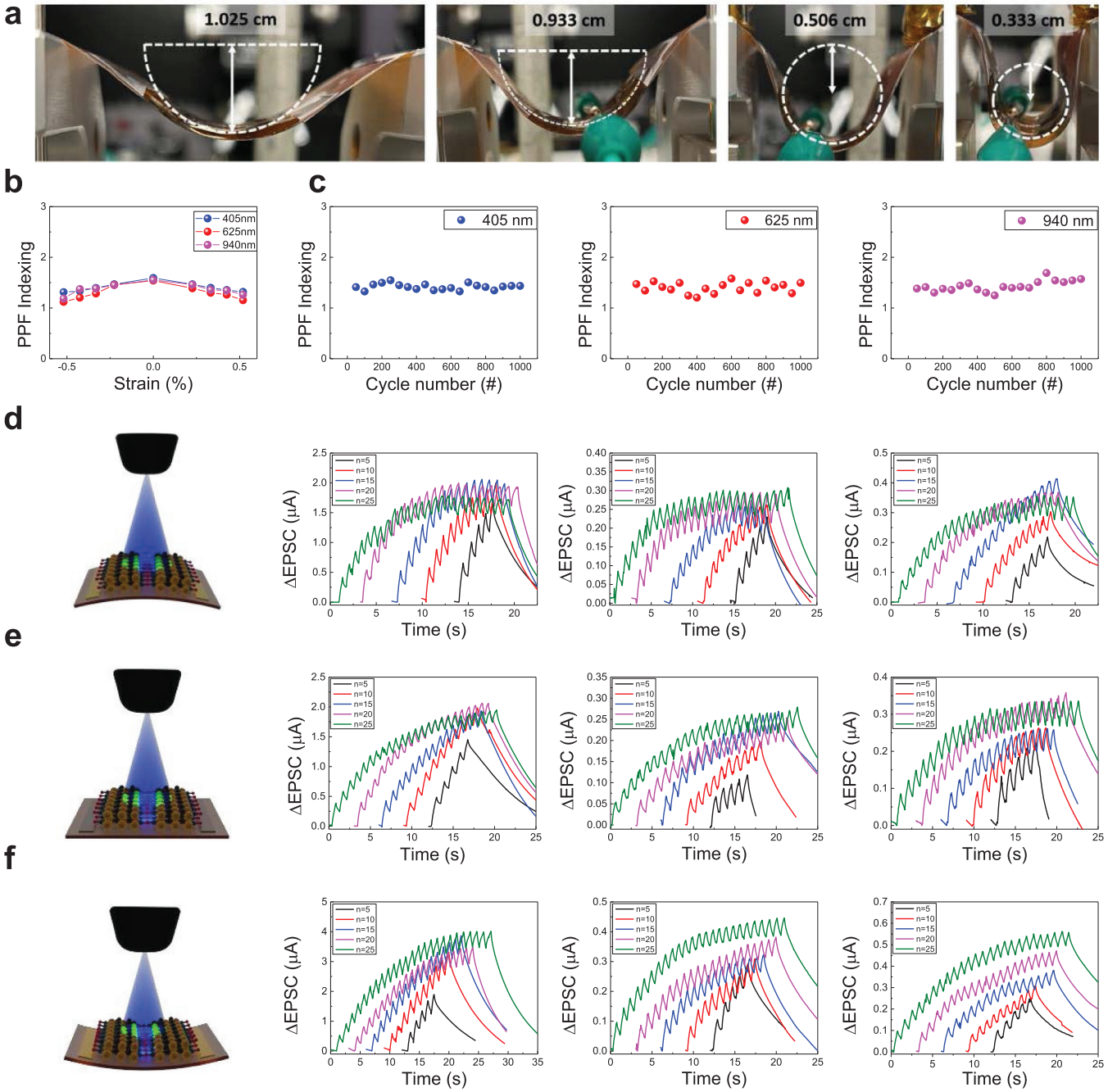

Fig. 3. Mechanical robustness of flexible $Ti_3C_2T_x$-based optoelectronic devices. (a) Snapshot images of flexible devices under harsh bending with various bending radius values. (b) Relationship between PPF indexing and bending strain obtained at wavelengths of 405 nm, 625 nm, and 940 nm. (c) PPF indexing of flexible $Ti_3C_2T_x$-based device under cyclic bending/releasing tests corresponding to wavelengths of; 405 nm (left), 625 nm (middle), and 940 nm (right). (d) Schematic of the bent state of the flexible $Ti_3C_2T_x$-based device and STP, LTD characteristics for pulse numbers of n = 5, 10, 15, 20, 25 under optical illuminations at wavelengths of; 405 nm (left), 625 nm (middle), and 940 nm (right). (e) Schematic of the flat state of the flexible $Ti_3C_2T_x$-based device and STP, LTD characteristics for pulse numbers of n = 5, 10, 15, 20, 25 under optical illuminations at wavelengths of; 405 nm (left), 625 nm (middle), and 940 nm (right). (f) Schematic of the folded state of the flexible $Ti_3C_2T_x$-based device and STP, LTD characteristics for pulse numbers of n = 5, 10, 15, 20, 25 under optical illuminations at wavelengths of; 405 nm (left), 625 nm (middle), and 940 nm (right).

bending radius of 1.03 cm, and its PPF indexing was determined at every 50 cycles. Fig. 3c depicts a trend of PPF indexing for the identical device at wavelengths of 405 (left), 625 (middle), and 940 nm (right), revealing well-retained characteristics irrespective of the wavelength variation. Throughout the harsh deformation tests, PPF indexing values were subtly changed, but retained a negligible difference of < 0.28. The STP and LTD characteristics were also observed in mechanically deformed flexible devices at states of bent (Fig. 3d), flat (Fig. 3e), and folded (Fig. 3f). The conditions were identical as Fig. 2; i.e. pulse numbers n = 5, 10, 15, 20, 25 and wavelengths of 405 nm (left), 625 nm (middle), and 940 nm (right). The flexible device shows consistent synaptic plasticity features irrelevant to the harshly deformed states of bending or folding. Furthermore, it is worth mentioning that the synaptic characteristics presented in Fig. 2 and Fig. 3 were obtained from separate devices fabricated in different batches. However, all these devices yield highly similar synaptic characteristics, which confirm low device-to-

device variations with high performance fidelity.

Image recognition demonstration of flexible $Ti_3C_2T_x$-based optoelectronic device for ANN applications

The deformation-invariant synaptic plasticity of MXene devices was employed to demonstrate flexible optoelectronic artificial synapses for practical neuromorphic applications. Specifically, we demonstrated ANN applications by investigating the pattern/image recognition accuracy of the devices in physically deformed forms. For this, flexible devices were optically potentiated and electrically depressed by a number of optical and electrical pulse cycles, respectively. This operation ensures a statistically reliable quantity of datasets for extracting essential parameters such as synaptic weight non-linearity, cycle-to-cycle variations, maximum/minimum conductance ratios, and device-to-device variations. Neuromorphic pattern/image recognition simulations were conducted based on the Multi-Layer-Perceptron (MLP) neural network for data processing. Fig. 4a-c show LTP/LTD characteristics employed for the simulations, which are presented as representative examples selected from a large number of measurement data. The devices were optically potentiated and electrically depressed in three different states of flat (Fig. 4a), folded (Fig. 4b), and bent (Fig. 4c). The optical potentiation was performed with 940 nm pulses (interval: 500 ms, intensity: 320 W/m^2) and the electrical depression was implemented by negative (-1 mV) electrical pulses with 50 ms intervals. The pulse numbers for both potentiation/depressions were 30 times. The potentiation/depression tests used for the device's training of flat, folded, and bent state at wavelength 940 nm are shown in, Supporting Information, Fig. S3. For the demonstrations of the device's broadband-based pattern/image recognition ability, similar potentiation/depression tests were also performed at wavelengths of 405 nm (intensity: 30 W/m^2) and 625 nm (intensity: 150 W/m^2) in flat, folded, and bent states (Supporting Information, Fig. S4, and Fig. S5, respectively). One vital parameter to assess the learning ability of artificial synapses is the "non-linearity factor" which is defined in a behavioral model by Chen et al. [46]. A high accuracy process demands the non-linearity factor close to (or less than) unity, which corresponds to a high linearity in synaptic weight updates [47]. The non-linearity factor values were extracted using the following equations based on the experimental potentiation/depression curves;

$$G_{LTP} = B \bullet \left(1 - \exp\left(-\frac{P}{A_p}\right)\right) + G_{\min} \tag{2}$$

$$G_{LTD} = -B \bullet \left(1 - \exp\left(\frac{P - P_{\max}}{A_D}\right)\right) + G_{\max} \tag{3}$$

$$B = (G_{\max} - G_{\min}) \Big/ \left(1 - \exp\left(-\frac{P_{\max}}{A_{P,D}}\right)\right) \tag{4}$$

where G_{LTP}, G_{LTD} are the conductance values of LTP, LTD regions, G_{max}, G_{min} are the maximum, minimum conductance values in LTP, LTD, P is the applied pulse number, A is the parameter demonstrating the non-linearity, and B is defined to refine the equations of (2), (3). The derived non-linearity factor values are in a range of 1.169–1.247 for potentiation and −0.851 to −0.766 for depression, indicating that the devices exhibit favorable learning features. Fig. 4d (left) illustrates a schematic of the logistics employed for the pattern/image recognition simulations, where the synaptic weight is defined to be the conductance divergence of two identical optical synapses ($W_{nm} = G^{+}_{nm}$ - G^{-}_{nm}) updated by back-propagation [8,48]. A handwritten digit (28 × 28 pixels) derived from

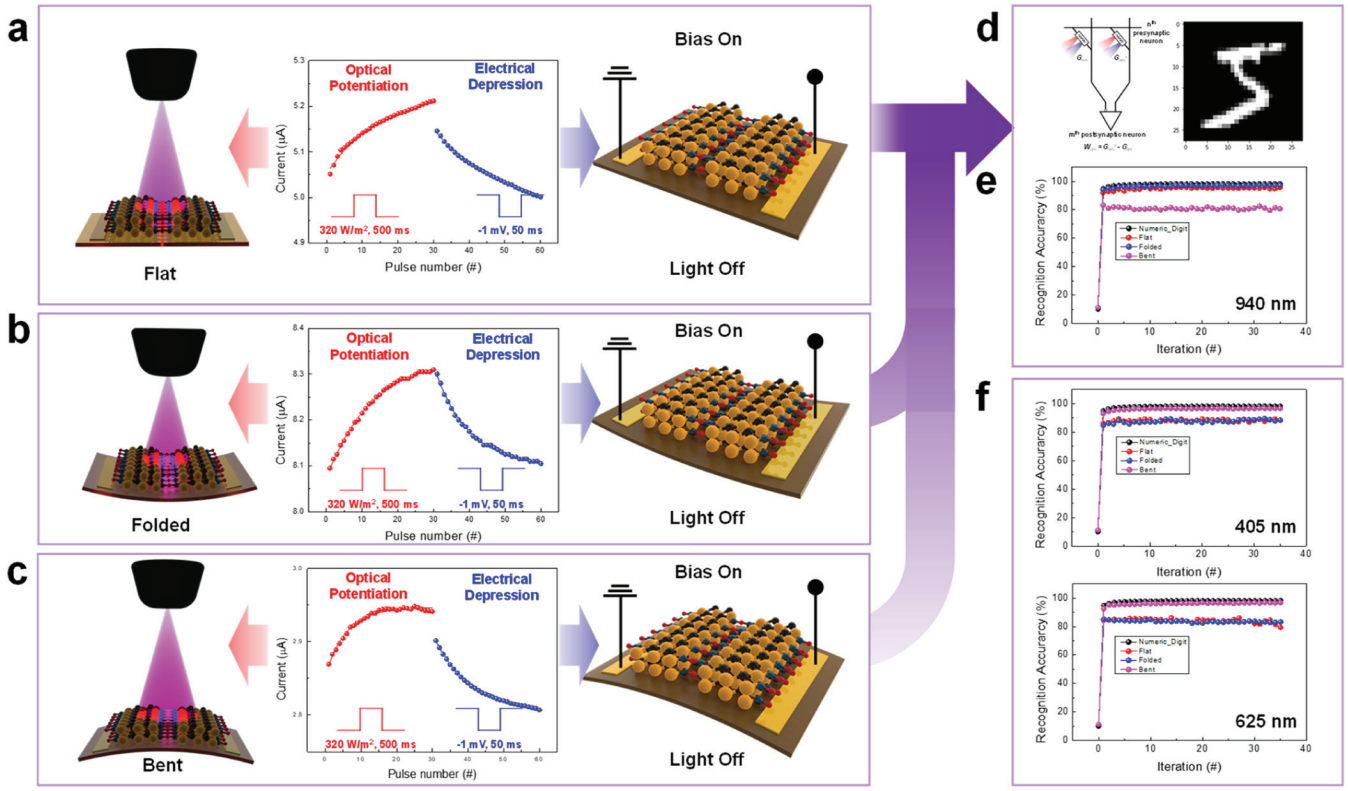

Fig. 4. Image recognition demonstration of flexible $Ti_3C_2T_x$-based optoelectronic device for ANN applications. (a-c) Representative LTP/LTD characteristics enabled by optical potentiation (wavelength: 940 nm, intensity: 320 W/m^2, interval: 500 ms) and electrical depression (bias: −1 mV, interval: 50 ms) in three different states of; (a) flat, (b) folded, and (c) bent. (d) Scheme illustration of image training principle (left), and MNIST letter image composed of 28 × 28 pixels employed for recognition accuracy tests (right). (e) Recognition accuracy plot obtained from (a) at a wavelength of 940 nm. (f) Recognition accuracy plots corresponding to wavelengths of 405 nm (top) and 625 nm (bottom). Accuracies of 88.47 % (flat), 88.29 % (folded), 96.5 % (bent) are observed for 405 nm, and 84.57 % (flat), 83.20 % (folded), 96.73 % (bent) are for 625 nm.

the Modified National Institute of Standards and Technology (MNIST) database (Fig. 4d (right)) was trained, and its recognition accuracy was evaluated using an ANN with three layers of input, hidden, and output. In the simulations, 60,000 handwritten image sets were utilized for training and 10,000 images were used for testing estimation. Fig. 4e presents the accuracy test result obtained at 940 nm wavelength, revealing that the device can precisely recognize the image irrespective of its deformation variation, i.e., 95.61 for flat, 97.13 for folded, and 80.68 % for bent states, respectively. Furthermore, the device was tested at other wavelengths under identical deformation conditions as well. Fig. 4f presents the corresponding recognition accuracy plots obtained at wavelengths of 405 (top) and 625 nm (bottom), respectively. Similar to the characteristics with 940 nm illuminations, the device exhibits fairly high accuracies of ~90 % regardless of the mechanical deformation.

Associative learning application and mechanism study of optical synaptic plasticity

Lastly, we demonstrate an additional application aspect of MXene devices in ANN and discuss their universal working principle for synaptic operations. Specifically, we explore their Pavlovian conditioning-based associative learning ability by training them under optically modulated conditions [49,50] (Fig. 5a). The device corresponding to Pavlov's dog is repeatedly stimulated by 625 nm pulses for 10 times with on/off intervals of 500 ms, which corresponds to the bell-conditioned stimulation. Subsequently, it is exposed to 405 nm pulses under the identical pulse duration/interval conditions, which function as food-unconditioned stimulation. In the Pavlovian conditioning, ringing the bell-only without other stimuli does not induce any responses from the dog while providing food will stimulate it to react by salivating. Once the dog is repeatedly trained with a simultaneous introduction of bell/food stimuli, it still responds to the bell-only stimuli without food even after the training is completed. However, after prolonging multiple sequences of the bell-only stimuli, the dog starts to forget the trained information and no longer reacts to the bell solitary process unless the food is again provided. In experimental demonstrations, the case of the dog's salivating upon food stimuli corresponds to that the device exhibits output currents surpassing a certain threshold conductance set by optical inputs. The device is initially trained with optical pulses of two different wavelengths, i.e., 625 nm for bell-only

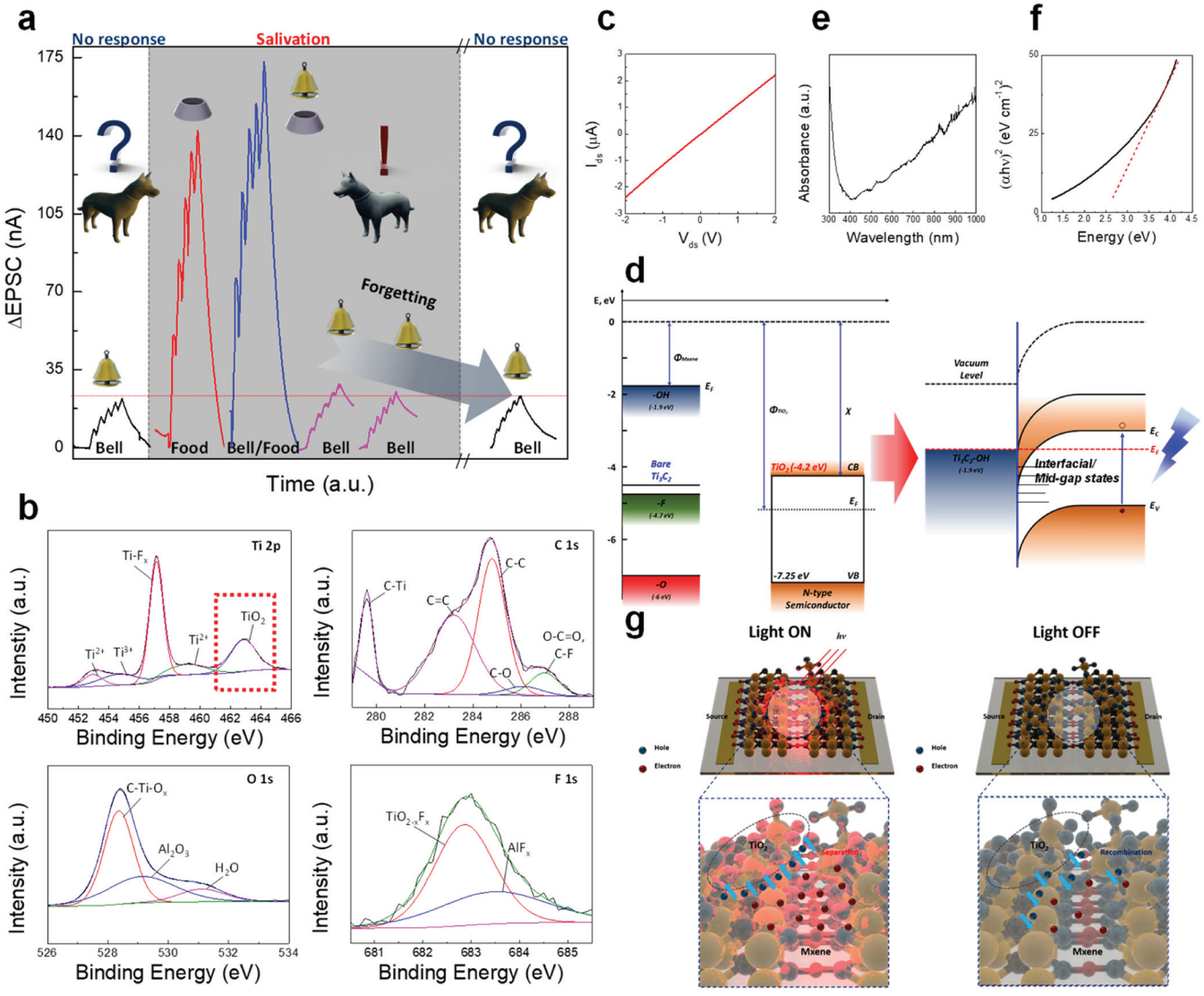

Fig. 5. Associative learning application and mechanism study of optical synaptic plasticity. (a) Pavlov's conditioning demonstration with paired pulses of 625 nm/405 nm for bell/food stimuli. (b) XPS spectra for Ti 2p, C 1 s, O 1 s, and F 1 s revealing TiO_2 phase. (c) *I-V* characteristics of Ohmic transport. (d) Band structures constructing Ohmic contact between TiO_2 and $Ti_3C_2T_x$. (e) UV-Vis absorbance spectrum. (f) Tauc plot corresponding to (e). (g) Schematic illustration of optical synaptic plasticity enabled by PPC effect.

(black curves) and 405 nm for food-only (red curves) stimuli, respectively. During this training period (gray shaded area), it constantly exhibits output currents (ΔEPSC values) higher than the threshold current denoted by the red dotted horizontal line. Even after the training is terminated, the device initially presents ΔEPSC values still exceeding the threshold current under bell-only stimuli (purple curves). Ultimately, it exhibits ΔEPSC values below the threshold value upon the iterative bell-only stimuli, which corresponds to the forgetting process of the Pavlovian's dog (last black curve). To further leverage the optically-induced threshold operations of MXene devices, simple logic gate tests were conducted in realizing "OR" and "AND" operations, as demonstrated in Supporting Information, Fig. S6. In these operations, the threshold current values set by optical stimuli define the operation conditions of an optically-modulated device, i.e., the device functions (ON) upon exceeding a threshold current while it becomes deactivated (OFF) when yielding an output current below the threshold value. The AND operation is implemented only when both stimuli (i.e., 405 nm "and" 625 nm wavelengths) are introduced, while the OR operation is possible with an application of any stimuli (i.e., 940 nm "or" 405 nm wavelengths). Comprehensive observations of the synaptic characteristics in MXenes and their neuromorphic applications allow us to investigate the fundamental mechanism behind the optically-modulated potentiation/depression. Particularly, while $Ti_3C_2T_x$-based MXenes are generally believed to be metallic [51], it is interesting to note that our devices exhibit strong photo-responsiveness with memory effects, a typical feature of certain semiconductors with intrinsic persistent photoconductivity (PPC) [52]. To unveil the origin for the projected semiconducting nature of our materials, we performed X-ray photoelectron spectroscopy (XPS) characterizations and identified their molecular structures. Fig. 5b presents XPS core-level binding energy spectra of Ti 2p, C 1 s, O 1 s, and F 1 s obtained from a representative sample. Notably, stoichiometrically matched titanium dioxide (TiO_2) peaks (red box in the first plot) are observed, indicating the presence of crystalline TiO_2 phases within MXenes [33,53–55]. This observation is attributed to a spontaneous oxidation of Ti introduced through MXene processing steps, which well agrees with previous reports on the strong tendency for a partial/natural oxidation of Ti within $Ti_3C_2T_x$ [56,57]. This analysis suggests that our optically synaptic MXenes should be in a heterogeneous form of MXene/TiO_2 composites where the stoichiometric TiO_2 is projected to retain its own semiconducting characteristics to a certain degree [33,58]; i.e., it is known to be an *n*-type semiconductor with a bandgap of ~3 eV [59,60]. For further verification, we performed two-terminal current-voltage (*I-V*) characterizations of our materials and identified highly Ohmic characteristics (Fig. 5c). Such Ohmic transports are typically observed irrespective of repetitive measurements at multiple locations, which indicates a high feasibility of forming Ohmic contacts between MXene and TiO_2 [57,61,62]. Based on this analysis, we constructed energy bands of the MXene/TiO_2 heterostructure by utilizing the material parameters available in literature [57], as presented in Fig. 5d. The work function of MXene is known to strongly depend on the variation of its functional groups such as -OH, -F, and -O, as clarified in Fig. 5d (left). We discuss the scenario of Ohmic contacts at the MXene (metallic)/TiO_2 (semiconducting) interfaces, which corresponds to the case that OH-terminated functional groups dominate within MXenes, as shown in Fig. 5d (right). In this band bending structure, it is highly likely that photo-excited charge carriers from the semiconducting TiO_2 will contribute to generating the positive photo-responsiveness [33,58], as observed in our experiments. Additionally, the chemical solution-based MXene processing is known to intrinsically introduce a large degree of structural/chemical imperfections into resulting materials [63]; e.g., functional groups, grain boundaries, vacancies, etc. These additional variations are believed to significantly influence the photo-excited carrier dynamics, thus introducing the PPC effect into the materials (to be discussed later). To verify the naturally-formed semiconducting nature of our MXenes, we employed ultraviolet-visible (UV–vis) spectroscopy characterizations and their associated Tauc plot measurements. Fig. 5e presents a UV–vis spectrum of a representative sample, and Fig. 5f shows the corresponding Tauc plot extracted from the spectrum, yielding its optical bandgap energy from the linear extrapolation intercepting the x-axis. The tangential line to the plot is selected in the linear regime corresponding to the photon energy of < 3.0 eV, consistent with previous approaches [64,65]. Although it is difficult to pinpoint the exact bandgap energy due to the uncertainty of precisely defining the linearity, it is obvious that the material is semiconducting, indicating the presence of TiO_2 phases. For further assessments of the band structure of the semiconducting MXene materials, we employed photoluminescence (PL) characterizations. The PL spectrum presented in Supporting Information Fig. S7 reveals a broad PL peak at a wavelength of ~600 nm which corresponds to a photon energy of ~2.0 eV. The peak position is observed to be slightly red-shifted compared to those observed with pristine $Ti_3C_2T_x$ MXenes in quantum dot forms [66] as well as $Ti_3C_2T_x$-based MXene composites [67,68]. Such shifts and/or appearances of additional PL peaks are generally attributed to the interband transition-related radiative recombination of charge carriers in defective semiconductors [69], which reflects the defective nature of our MXene materials introduced by TiO_2 phases. Fig. 5g illustrates the proposed mechanism for the optical synapses of semiconducting MXenes based on the defects-mediated PPC model. Upon optical illuminations, the photo-excited carriers generated from the TiO_2-associated components within MXenes transport to overcome their bandgap energy. Due to the abundant defects introduced by their solution processability, a portion of the charge carriers are trapped at the interfacial/mid-gap states of the bandgap (Fig. 5f right), causing a slow generation of photocurrents. Once the illuminations are terminated, the excited free carriers as well as the trapped carriers relax through de-excitations and transport toward their spontaneous recombination. These carriers undergo a significant delay in the recombination dynamics owing to the interfacial/mid-gap mediated trapping/de-trapping sequences, yielding a slow decay of photocurrents [70]. Lastly, we highlight novel aspects of our MXene artificial synapses in the context of their broadband-responsive optical operation and mechanical flexibility. These features clearly differentiate them from previous developments of MXene-based synaptic devices which generally employ solitary electrical pulses and rigid substrates, as comprehensively compared in Table 1. Finally, it is worth mentioning that the performance of our optically operational synaptic devices can be further improved by optimizing the relative concentration of MXene/TiO_2, i.e., ratio of metallic/semiconducting components, which should be possible with adjusting the MXene processing conditions.

Conclusion

In conclusion, this study highlights relatively unexplored aspects of MXenes for optoelectronic artificial synapses and their flexible device applications in neuromorphic computing. Major findings of the study suggest a substantial milestone of MXenes as optically/mechanically-coupled device building blocks beyond the conventional von Neumann logistics. This device also is anticipated to be developed as a realized optical synaptic device by fabricating an array optimizing the facile liquid process by simply dropping MXene and applying electrodes onto a large flexible substrate. Furthermore, the study is believed to significantly broaden the versatility and prospects of other non-covalently bonded layered materials toward their integration into transformative neuromorphic architectures. The MXene devices explored in this study are also suitable for realizing large-area scaled-up optical synapse arrays owing to their intrinsic fabrication advantages of simple drop-casting procedures for MXenes as well as their compatibility with arbitrary substrates.

Table 1
Comparison table of MXene-based artificial synapses.

Material	Operational Mode	Operation Principle	Device structure	Accuracy (%)	Non-linearity	Reference
$Ti_3C_2T_x$	Electrical Pulse	Resistive switching	2-terminal vertical rigid device	×	×	[71]
LPE/$Ti_3C_2T_x$	Electrical Pulse	Resistive switching	2-terminal vertical rigid device	×	×	[72]
$Ti_3C_2T_x$	Electrical Pulse	Resistive switching	2-terminal lateral rigid device	87.5	2.3, 1.9	[73]
ZTO/TiO_2/$Ti_3C_2T_x$	Optical Pulse/ Electrical Pulse	UV light/ Resistive switching	2-terminal vertical rigid device	83	0.73, 2.05	[74]
Ti_3C_2	Electrical Pulse	Resistive switching	2-terminal vertical rigid device	×	×	[75]
Ti_3C_2/FTO	Optical Pulse/ Electrical Pulse	NIR/Resistive switching	2-terminal vertical rigid device	×	×	[76]
Ti_3C_2/TAPA	Optical Pulse	Resistive switching	3-terminal lateral rigid FET	93	1.5, 2.8	[77]
Ti_3C_2/NiO/FTO	Electrical Pulse	Resistive switching	2-terminal vertical rigid device	96.8	2.85, 3.34	[78]
Ti_3C_2	Electrical Pulse	Resistive switching	2-terminal vertical rigid device	×	×	[79]
TiO_2-incorporated $Ti_3C_2T_x$	**Optical Pulse/ Electrical Pulse**	**Visible-to-NIR broadband light**	**2-terminal lateral flexible device**	96.73	1.169, −0.851	**Our Work**

CRediT authorship contribution statement

Changhyeon Yoo: Validation, Software, Resources, Formal analysis. **Seung Ju Kim:** Visualization, Software, Methodology, Investigation, Data curation, Conceptualization. **Chung Won Lee:** Writing – review & editing, Writing – original draft, Visualization, Validation, Software, Resources, Methodology, Investigation, Formal analysis, Data curation, Conceptualization. **Young-Jun Cho:** Visualization, Validation, Methodology, Investigation, Data curation. **Han-Kyun Shin:** Visualization, Validation, Software, Investigation, Data curation. **Yeonwoong Jung:** Writing – review & editing, Writing – original draft, Visualization, Validation, Supervision, Resources, Investigation, Funding acquisition, Data curation, Conceptualization. **Jung Han Kim:** Visualization, Validation, Supervision, Software, Investigation, Data curation. **Hyo-Jong Lee:** Validation, Supervision, Investigation, Data curation. **Sang Sub Han:** Visualization, Investigation, Formal analysis, Data curation.

Declaration of Competing Interest

The authors declare that they have no known competing financial interests or personal relationships that could have appeared to influence the work reported in this paper.

Acknowledgments

Y. J. acknowledges financial support from the US National Science Foundation (CAREER: 2142310). S. S. H. acknowledges financial support from the Preeminent Postdoctoral Program (P3) at UCF. J. H. K. acknowledges support from the National Research Foundation (NRF) funded by the Korean government (MSIT) (No. RS-2024-00426823).

Appendix A. Supporting information

Supplementary data associated with this article can be found in the online version at doi:10.1016/j.nantod.2025.102633.

Data availability

Data will be made available on request.

References

[1] S.J. Kim, I.H. Im, J.H. Baek, S. Choi, S.H. Park, D.E. Lee, J.Y. Kim, S.Y. Kim, N.-G. Park, D. Lee, Linearly programmable two-dimensional halide perovskite memristor arrays for neuromorphic computing, Nat. Nanotechnol. (2024) 1–10.
[2] C. Wu, T.W. Kim, H.Y. Choi, D.B. Strukov, J.J. Yang, Flexible three-dimensional artificial synapse networks with correlated learning and trainable memory capability, Nat. Commun. 8 (2017) 752.
[3] C. Liu, X. Yan, X. Song, S. Ding, D.W. Zhang, P. Zhou, A semi-floating gate memory based on van der Waals heterostructures for quasi-non-volatile applications, Nat. Nanotechnol. 13 (2018) 404–410.
[4] S. Manipatruni, D.E. Nikonov, I.A. Young, Beyond CMOS computing with spin and polarization, Nat. Phys. 14 (2018) 338–343.
[5] M. Kumar, J. Kim, C.-P. Wong, Transparent and flexible photonic artificial synapse with piezo-phototronic modulator: versatile memory capability and higher order learning algorithm, Nano Energy 63 (2019) 103843.
[6] T.Y. Wang, J.L. Meng, Z.Y. He, L. Chen, H. Zhu, Q.Q. Sun, S.J. Ding, P. Zhou, D. W. Zhang, Ultralow power wearable heterosynapse with photoelectric synergistic modulation, Adv. Sci. 7 (2020) 1903480.
[7] N. Duan, Y. Li, H.-C. Chiang, J. Chen, W.-Q. Pan, Y.-X. Zhou, Y.-C. Chien, Y.-H. He, K.-H. Xue, G. Liu, An electro-photo-sensitive synaptic transistor for edge neuromorphic visual systems, Nanoscale 11 (2019) 17590–17599.
[8] S. Seo, B.-S. Kang, J.-J. Lee, H.-J. Ryu, S. Kim, H. Kim, S. Oh, J. Shim, K. Heo, S. Oh, Artificial van der Waals hybrid synapse and its application to acoustic pattern recognition, Nat. Commun. 11 (2020) 3936.
[9] S. Yu, B. Gao, Z. Fang, H. Yu, J. Kang, H.S.P. Wong, A low energy oxide-based electronic synaptic device for neuromorphic visual systems with tolerance to device variation, Adv. Mater. 25 (2013) 1774–1779.
[10] S. Seo, S.-H. Jo, S. Kim, J. Shim, S. Oh, J.-H. Kim, K. Heo, J.-W. Choi, C. Choi, S. Oh, Artificial optic-neural synapse for colored and color-mixed pattern recognition, Nat. Commun. 9 (2018) 5106.
[11] F. Zhou, Z. Zhou, J. Chen, T.H. Choy, J. Wang, N. Zhang, Z. Lin, S. Yu, J. Kang, H.-S.P. Wong, Optoelectronic resistive random access memory for neuromorphic vision sensors, Nat. Nanotechnol. 14 (2019) 776–782.
[12] S. Dai, Y. Zhao, Y. Wang, J. Zhang, L. Fang, S. Jin, Y. Shao, J. Huang, Recent advances in transistor-based artificial synapses, Adv. Funct. Mater. 29 (2019) 1903700.
[13] W. Huh, D. Lee, C.H. Lee, Memristors based on 2D materials as an artificial synapse for neuromorphic electronics, Adv. Mater. 32 (2020) 2002092.
[14] C.W. Lee, C. Yoo, S.S. Han, Y.-J. Song, S.J. Kim, J.H. Kim, Y. Jung, Centimeter-scale tellurium oxide films for artificial optoelectronic synapses with broadband responsiveness and mechanical flexibility, ACS Nano 18 (2024) 18635–18649.
[15] T. Ahmed, S. Kuriakose, E.L. Mayes, R. Ramanathan, V. Bansal, M. Bhaskaran, S. Sriram, S. Walia, Optically stimulated artificial synapse based on layered black phosphorus, Small 15 (2019) 1900966.
[16] C.M. Yang, T.C. Chen, D. Verma, L.J. Li, B. Liu, W.H. Chang, C.S. Lai, Bidirectional all-optical synapses based on a 2D Bi_2O_2Se/graphene hybrid structure for multifunctional optoelectronics, Adv. Funct. Mater. 30 (2020) 2001598.
[17] J. Meng, T. Wang, H. Zhu, L. Ji, W. Bao, P. Zhou, L. Chen, Q.-Q. Sun, D.W. Zhang, Integrated in-sensor computing optoelectronic device for environment-adaptable artificial retina perception application, Nano Lett. 22 (2021) 81–89.
[18] Y. Li, J. Wang, Q. Yang, G. Shen, Flexible artificial optoelectronic synapse based on lead-free metal halide nanocrystals for neuromorphic computing and color recognition, Adv. Sci. 9 (2022) 2202123.
[19] R. Ji, G. Feng, C. Jiang, B. Tian, C. Luo, H. Lin, X. Tang, H. Peng, C.G. Duan, Fully light-modulated organic artificial synapse with the assistance of ferroelectric polarization, Adv. Electron. Mater. 8 (2022) 2101402.
[20] D. Hao, Z. Yang, J. Huang, F. Shan, Recent developments of optoelectronic synaptic devices based on metal halide perovskites, Adv. Funct. Mater. 33 (2023) 2211467.
[21] M. Magnuson, M. Mattesini, Chemical bonding and electronic-structure in MAX phases as viewed by X-ray spectroscopy and density functional theory, Thin Solid Films 621 (2017) 108–130.
[22] K.R.G. Lim, M. Shekhirev, B.C. Wyatt, B. Anasori, Y. Gogotsi, Z.W. Seh, Fundamentals of MXene synthesis, Nat. Synth. 1 (2022) 601–614.
[23] M. Khazaei, A. Ranjbar, M. Arai, T. Sasaki, S. Yunoki, Electronic properties and applications of MXenes: a theoretical review, J. Mater. Chem. C 5 (2017) 2488–2503.
[24] A. Enyashin, A. Ivanovskii, Two-dimensional titanium carbonitrides and their hydroxylated derivatives: structural, electronic properties and stability of MXenes $Ti_3C_{2-x}N_x(OH)_2$ from DFTB calculations, J. Solid State Chem. 207 (2013) 42–48.
[25] G. Ding, B. Yang, R.-S. Chen, K. Zhou, S.-T. Han, Y. Zhou, MXenes for memristive and tactile sensory systems, Appl. Phys. Rev. 8 (2021).
[26] L. Guo, B. Mu, M.-Z. Li, B. Yang, R.-S. Chen, G. Ding, K. Zhou, Y. Liu, C.-C. Kuo, S.-T. Han, Stacked two-dimensional MXene composites for an energy-efficient memory and digital comparator, ACS Appl. Mater. Interfaces 13 (2021) 39595–39605.
[27] A. Sarycheva, Y. Gogotsi, Raman spectroscopy analysis of the structure and surface chemistry of Ti3C2T x MXene, Chem. Mater. 32 (2020) 3480–3488.

[28] T. Hu, M. Hu, B. Gao, W. Li, X. Wang, Screening surface structure of MXenes by high-throughput computation and vibrational spectroscopic confirmation, J. Phys. Chem. C 122 (2018) 18501–18509.

[29] A.A. Emerenciano, R.M. do Nascimento, A.P.C. Barbosa, K. Ran, W.A. Meulenberg, J. Gonzalez-Julian, Ti3C2 MXene membranes for gas separation: influence of heat treatment conditions on D-spacing and surface functionalization, Membranes 12 (2022) 1025.

[30] H. Alnoor, A. Elsukova, J. Palisaitis, I. Persson, E.N. Tseng, J. Lu, L. Hultman, P. Å. Persson, Exploring MXenes and their MAX phase precursors by electron microscopy, Mater. Today Adv. 9 (2021) 100123.

[31] R. Liu, W. Li, High-thermal-stability and high-thermal-conductivity $Ti_3C_2T_x$ MXene/poly (vinyl alcohol)(PVA) composites, ACS Omega 3 (2018) 2609–2617.

[32] Y. Li, D. Zhang, X. Feng, Y. Liao, Q. Wen, Q. Xiang, Truncated octahedral bipyramidal TiO $_2$/MXene Ti_3C_2 hybrids with enhanced photocatalytic H_2 production activity, Nanoscale Adv. 1 (2019) 1812–1818.

[33] J. Low, L. Zhang, T. Tong, B. Shen, J. Yu, TiO_2/MXene Ti_3C_2 composite with excellent photocatalytic CO2 reduction activity, J. Catal. 361 (2018) 255–266.

[34] S. Zong, J. Liu, Z. Huang, L. Liu, J. Liu, J. Zheng, Y. Fang, Mxene-TiO_2 composite with exposed {101} facets for the improved photocatalytic hydrogen evolution activity, J. Alloy Compd. 896 (2022) 163039.

[35] L. Chen, K. Huang, Q. Xie, S.M. Lam, J.C. Sin, T. Su, H. Ji, Z. Qin, The enhancement of photocatalytic CO_2 reduction by the in situ growth of TiO_2 on Ti_3C_2 MXene, Catal. Sci. Technol. 11 (2021) 1602–1614.

[36] R.A. Soomro, J. Kumar, R.R. Neiber, A.M. Alotaibi, S.F. Shaikh, N. Ahmed, A. Nafady, Natural oxidation of Ti3C2Tx to construct efficient TiO_2/$Ti_3C_2T_x$ photoactive heterojunctions for advanced photoelectrochemical biosensing of folate-expressing cancer cells, Anal. Chim. Acta 1251 (2023) 341016.

[37] F. Xia, J. Lao, R. Yu, X. Sang, J. Luo, Y. Li, J. Wu, Ambient oxidation of Ti_3C_2 MXene initialized by atomic defects, Nanoscale 11 (2019) 23330–23337.

[38] R.C. Atkinson, R.M. Shiffrin, Human memory: A proposed system and its control processes. Psychology of learning and motivation, Elsevier, 1968, pp. 89–195.

[39] T. Chang, S.-H. Jo, W. Lu, Short-term memory to long-term memory transition in a nanoscale memristor, ACS Nano 5 (2011) 7669–7676.

[40] Y. Liu, Y. Wu, H. Han, Y. Wang, R. Peng, K. Liu, D. Yi, C.W. Nan, J. Ma, $CuInP_2S_6$-based electronic/optoelectronic synapse for artificial visual system application, Adv. Funct. Mater. 34 (2024) 2306945.

[41] Y. Guo, F. Wu, G.H. Dun, T. Cui, Y. Liu, X. Tan, Y. Qiao, M. Lanza, H. Tian, Y. Yang, Electrospun nanofiber-based synaptic transistor with tunable plasticity for neuromorphic computing, Adv. Funct. Mater. 33 (2023) 2208055.

[42] L. Wang, C. Zheng, J. Fu, J. Hua, J. Chen, J. Gao, H. Ling, L. Xie, W. Huang, Influence of molecular weight of polymer electret on the synaptic organic field-effect transistor performance, Adv. Electron. Mater. 8 (2022) 2200155.

[43] H. Ling, N. Wang, A. Yang, Y. Liu, J. Song, F. Yan, Dynamically reconfigurable short-term synapse with millivolt stimulus resolution based on organic electrochemical transistors, Adv. Mater. Technol. 4 (2019) 1900471.

[44] S. Dai, X. Wu, D. Liu, Y. Chu, K. Wang, B. Yang, J. Huang, Light-stimulated synaptic devices utilizing interfacial effect of organic field-effect transistors, ACS Appl. Mater. Interfaces 10 (2018) 21472–21480.

[45] B.H. Jeong, J. Park, D. Kim, J. Lee, I.H. Jung, H.J. Park, Visible light-sensitive artificial photonic synapse, Adv. Opt. Mater. 12 (2024) 2301652.

[46] P.-Y. Chen, B. Lin, I.-T. Wang, T.-H. Hou, J. Ye, S. Vrudhula, J.-s Seo, Y. Cao, S. Yu, Mitigating effects of non-ideal synaptic device characteristics for on-chip learning. 2015 IEEE/ACM International Conference on Computer-Aided Design (ICCAD), IEEE, 2015, pp. 194–199.

[47] C.-C. Chang, P.-C. Chen, T. Chou, I.-T. Wang, B. Hudec, C.-C. Chang, C.-M. Tsai, T.-S. Chang, T.-H. Hou, Mitigating asymmetric nonlinear weight update effects in hardware neural network based on analog resistive synapse, IEEE CASS 8 (2017) 116–124.

[48] J. Kim, S. Song, J.M. Lee, S. Nam, J. Kim, D.K. Hwang, S.K. Park, Y.H. Kim, Metal-oxide heterojunction optoelectronic synapse and multilevel memory devices enabled by broad spectral photocarrier modulation, Small 19 (2023) 2301186.

[49] T. Crow, Pavlovian conditioning of Hermissenda: current cellular, molecular, and circuit perspectives, Learn. Mem. 11 (2004) 229–238.

[50] K. Moon, S. Park, J. Jang, D. Lee, J. Woo, E. Cha, S. Lee, J. Park, J. Song, Y. Koo, Hardware implementation of associative memory characteristics with analogue-type resistive-switching device, Nanotechnology 25 (2014) 495204.

[51] S.J. Kim, H.-J. Koh, C.E. Ren, O. Kwon, K. Maleski, S.-Y. Cho, B. Anasori, C.-K. Kim, Y.-K. Choi, J. Kim, Metallic Ti3C2T x MXene gas sensors with ultrahigh signal-to-noise ratio, ACS Nano 12 (2018) 986–993.

[52] H. Ma, H. Fang, X. Xie, Y. Liu, H. Tian, Y. Chai, Optoelectronic synapses based on MXene/violet phosphorus van der waals heterojunctions for visual-olfactory crossmodal perception, Nanomicro Lett. 16 (2024) 104.

[53] H. Huang, Y. Song, N. Li, D. Chen, Q. Xu, H. Li, J. He, J. Lu, One-step in-situ preparation of N-doped TiO_2@C derived from Ti_3C_2 MXene for enhanced visible-light driven photodegradation, Appl. Catal. B 251 (2019) 154–161.

[54] X. Han, L. An, Y. Hu, Y. Li, C. Hou, H. Wang, Q. Zhang, Ti3C2 MXene-derived carbon-doped TiO2 coupled with g-C3N4 as the visible-light photocatalysts for photocatalytic H_2 generation, Appl. Catal. B 265 (2020) 118539.

[55] L. Deng, B. Chang, D. Shi, X. Yao, Y. Shao, J. Shen, B. Zhang, Y. Wu, X. Hao, MXene decorated by phosphorus-doped TiO2 for photo-enhanced electrocatalytic hydrogen evolution reaction, Renew. Energy 170 (2021) 858–865.

[56] W.-X. Huang, Z.-P. Li, D.-D. Li, Z.-H. Hu, C. Wu, K.-L. Lv, Q. Li, Ti3C2 MXene: recent progress in its fundamentals, synthesis, and applications, Rare Met. 41 (2022) 3268–3300.

[57] S. Chertopalov, V.N. Mochalin, Environment-sensitive photoresponse of spontaneously partially oxidized Ti3C2 MXene thin films, ACS Nano 12 (2018) 6109–6116.

[58] J.-X. Yang, W.-B. Yu, C.-F. Li, W.-D. Dong, L.-Q. Jiang, N. Zhou, Z.-P. Zhuang, J. Liu, Z.-Y. Hu, H. Zhao, PtO nanodots promoting Ti_3C_2 MXene in-situ converted Ti_3C_2/TiO_2 composites for photocatalytic hydrogen production, Chem. Eng. J. 420 (2021) 129695.

[59] L. Forro, O. Chauvet, D. Emin, L. Zuppiroli, H. Berger, F. Levy, High mobility n-type charge carriers in large single crystals of anatase (TiO_2), J. Appl. Phys. 75 (1994) 633–635.

[60] D.J. Mowbray, J.I. Martinez, J. García Lastra, K.S. Thygesen, K.W. Jacobsen, Stability and electronic properties of TiO_2 nanostructures with and without B and N doping, J. Phys. Chem. C 113 (2009) 12301–12308.

[61] C. Peng, P. Wei, X. Li, Y. Liu, Y. Cao, H. Wang, H. Yu, F. Peng, L. Zhang, B. Zhang, High efficiency photocatalytic hydrogen production over ternary Cu/TiO_2@ $Ti_3C_2T_x$ enabled by low-work-function 2D titanium carbide, Nano Energy 53 (2018) 97–107.

[62] R. Li, X. Ma, J. Li, J. Cao, H. Gao, T. Li, X. Zhang, L. Wang, Q. Zhang, G. Wang, Flexible and high-performance electrochromic devices enabled by self-assembled 2D TiO_2/MXene heterostructures, Nat. Commun. 12 (2021) 1587.

[63] K.P. Marquez, K.M.D. Sisican, R.P. Ibabao, R.A.J. Malenab, M.A.N. Judicpa, L. Henderson, J. Zhang, K.A.S. Usman, J.M. Razal, Understanding the chemical degradation of $Ti_3C_2T_x$ MXene dispersions: a chronological analysis, Small Sci. (2024) 2400150.

[64] A.B. Tambe, S.S. Arbuj, G.G. Umarji, N.S. Jawale, S.B. Rane, S.K. Kulkarni, B. B. Kale, 2D layered MXene/TiO_2 nano-heterostructures for photocatalytic H_2 generation, Graph. 2D Mater. 7 (2022) 91–106.

[65] A.A. Khan, M. Tahir, Well-designed 2D/2D Ti_3C_2TA/R MXene coupled g-C_3N_4 heterojunction with in-situ growth of anatase/rutile TiO_2 nucleates to boost photocatalytic dry-reforming of methane (DRM) for syngas production under visible light, Appl. Catal. B 285 (2021) 119777.

[66] Y. Feng, F. Zhou, Q. Deng, C. Peng, Solvothermal synthesis of in situ nitrogen-doped Ti_3C_2 MXene fluorescent quantum dots for selective Cu^{2+} detection, Ceram. Int. 46 (2020) 8320–8327.

[67] Y. Li, M. Zhang, Y. Liu, Q. Zhao, X. Li, Q. Zhou, Y. Chen, S. Wang, Construction of bronze TiO_2/Ti_3C_2 MXene/Ag_3PO_4 ternary composite photocatalyst toward high photocatalytic performance, Catal 12 (2022) 599.

[68] A.A. Alothman, M.R. Khan, M.D. Albaqami, S. Mohandoss, Z.A. Alothman, N. Ahmad, K.N. Alqahtani, Ti_3C_2-MXene/NiO nanocomposites-decorated $CsPbI_3$ perovskite active materials under UV-light irradiation for the enhancement of crystal-violet dye photodegradation, Nanomater 13 (2023) 3026.

[69] I. Levine, D. Menzel, A. Musiienko, R. MacQueen, N. Romano, M. Vasquez-Montoya, E. Unger, C. Mora Perez, A. Forde, A.J. Neukirch, Revisiting sub-band gap emission mechanism in 2D halide perovskites: the role of defect states, J. Am. Chem. Soc. 146 (2024) 23437–23448.

[70] L.V. Scalvi, C.F. Bueno, Transient decay of photoinduced current in semiconductors and heterostructures, J. Phys. D: Appl. Phys. 53 (2019) 033001.

[71] X. Yan, K. Wang, J. Zhao, Z. Zhou, H. Wang, J. Wang, L. Zhang, X. Li, Z. Xiao, Q. Zhao, A new memristor with 2D $Ti_3C_2T_x$ MXene flakes as an artificial bio-synapse, Small 15 (2019) 1900107.

[72] H. Wei, H. Yu, J. Gong, M. Ma, H. Han, Y. Ni, S. Zhang, W. Xu, Redox MXene artificial synapse with bidirectional plasticity and hypersensitive responsibility, Adv. Funct. Mater. 31 (2021) 2007232.

[73] J.H. Ju, S. Seo, S. Baek, D. Lee, S. Lee, T. Lee, B. Kim, J.J. Lee, J. Koo, H. Choo, Two-dimensional MXene synapse for brain-inspired neuromorphic computing, Small 17 (2021) 2102595.

[74] T. Zhao, C. Zhao, W. Xu, Y. Liu, H. Gao, I.Z. Mitrovic, E.G. Lim, L. Yang, C.Z. Zhao, Bio-inspired photoelectric artificial synapse based on two-dimensional $Ti_3C_2T_x$ MXenes floating gate, Adv. Funct. Mater. 31 (2021) 2106000.

[75] A. Sokolov, M. Ali, H. Li, Y.R. Jeon, M.J. Ko, C. Choi, Partially oxidized MXene $Ti_3C_2T_x$ sheets for memristor having synapse and threshold resistive switching characteristics, Adv. Electron. Mater. 7 (2021) 2000866.

[76] L. Yue, H. Sun, Y. Zhu, Y. Li, F. Yang, X. Dong, J. Chen, X. Zhang, J. Chen, Y. Zhao, Electrical-light coordinately modulated synaptic memristor based on Ti_3C_2 MXene for near-infrared artificial vision applications, J. Phys. Chem. Lett. 15 (2024) 8667–8675.

[77] A. Melianas, M.A. Kang, A. VahidMohammadi, T.J. Quill, W. Tian, Y. Gogotsi, A. Salleo, M.M. Hamedi, High-speed ionic synaptic memory based on 2D titanium carbide MXene, Adv. Funct. Mater. 32 (2022) 2109970.

[78] J. Fang, Z. Tang, X.-Q. Li, Z.-Y. Fan, Y.-P. Jiang, Q.-X. Liu, X.-G. Tang, J.-M. Fan, J. Gao, J. Shang, Synaptic learning behavior and neuromorphic computing of Au/MXene/NiO/FTO artificial synapse, Appl. Phys. Lett. 123 (2023).

[79] N.B. Mullani, D.D. Kumbhar, D.H. Lee, M.J. Kwon, Sy Cho, N. Oh, E.T. Kim, T. D. Dongale, S.Y. Nam, J.H. Park, Surface modification of a titanium carbide MXene memristor to enhance memory window and low-power operation, Adv. Funct. Mater. 33 (2023) 2300343.